13th ewtec 2019 Proceedings of the 13th European Wave and Tidal Energy Conference 1-6 Sept 2019, Naples, Italy

Numerical Simulation of Focused Wave Interaction with WECs using a Hybrid FNPT/NS Solver

Shiqiang Yan, Junxian Wang, Qingwei. Ma, Jinghua Wang, and Zhihua Xie

Abstract— **The paper presents a numerical investigation of the interaction between focused waves and wave energy convertors (WECs) using a hybrid model, qaleFOAM, which combines a two-phase Navier-Stokes model (NS) and the fully nonlinear potential theory (FNPT) using the spatially hierarchical approach. The former governs a limited computational domain (NS domain) around the structures, where the viscous effects are expected to be significant, and is solved by using OpenFOAM with a modified solver for the six degrees-of-freedom (6DoF) motions of rigid bodies. The latter covers the rest of the domain (FNPT domain) and is solved by using the Quasi Lagrangian Eulerian Finite Element Method (QALE-FEM). The WEC models, mooring system and the wave conditions are specified by the 2nd CCP-WSI (Collaborative Computational Project in Wave-Structure Interaction) Blind Test Workshop. In the numerical simulation, the incident wave is generated in the FNPT domain using a self-correction wavemaker and propagates into the NS domain through the coupling boundaries (inlet of the NS domain). An improved passive wave absorber is imposed on the outlet of the NS domain for the wave absorption. Its accuracy on generating incident waves is demonstrated by comparing its prediction with the experimental data in corresponding empty tank test. The motions of the WECs and the mooring forces are analysed.**

Keywords—**Wave-Structure Interaction, Focused Waves, WECs, Hybrid Model, CCP-WSI, Blind Test.**

I. Introduction

THE reliable prediction of the responses of the wave energy convertors (WECs) in waves plays an essential role on the design, deployment and operation of the WECs. For survivability of the WECs, its motions subjected to realistic extreme wave conditions need to be paid extra attention. Such extreme wave conditions are often generated in physical and numerical wave tanks using a focused wave group, e.g. the NewWave theory [1].

Paper ID 1452 submitted to conference track WHM. This work was supported in part by the EPSRC under grants EP/M022382, EP/N006569 and EP/N008863, and UKIERI-DST under grant DST-UKIERI-2016-17-0029.

S Yan, J.X. Wang, Q.W. Ma and J.H.Wang are at the School of Mathematics, Computer Science and Engineering, City, University of London (e-mail: shiqiang.yan@city.ac.uk). Z.H. Xie is with School of Engineering, Cardiff University(e-mail: zxie@cardiff.ac.uk).

For numerical predictions, numerous numerical models and software have been developed based on wide ranges of theoretical models, including the fully nonlinear potential theory (FNPT), where the fluid is assumed to be incompressible, irrotational and inviscid, and the single- or multi-phase Navier-Stokes (NS) models with or without turbulence modelling. The performances of these models in practices of the wave-structure interactions (WSI) are mainly affected by their effectiveness of generating the incident waves in the far field, modelling the wave propagation and its interaction with structures (including the motion of the structure) and resolving the turbulence/viscous effects, in the near field surrounding the structures. For the non-breaking extreme waves, it is widely accepted that the FNPT model can satisfactorily reproduce the wave conditions, as confirmed by [2-4]. For modelling the wave-structure interactions, the FNPT model can also deliver a promising accuracy if the structure is relatively big compared with the wave length [5-6], due to insignificant viscous effects involved in such problems. This was further confirmed by the final report of the first CCP-WSI (Collaborative Computational Project in Wave-Structure Interaction) blind test work organised in ISOPE 2018, in which cases with a fixed FPSO subjected to extreme wave conditions were numerically simulated using various numerical models and compared with the experimental data. Due to the fact that the experimental data of the blind test was released after the participators submitted their numerical predictions, minimizing the possibility of numerical calibrations or tuning. Thus, the performances of the participated numerical models can largely reflect their reliabilities in practices. One conclusion is that the accuracies of the FNPT models, such as the Quasi Lagrangian Eulerian Finite Element Method (QALE-FEM) [3-6], is at the similar level as the NS models, whereas the FNPT models require much less computer resources and CPU time [7-8]. Further analysis on [7] confirmed the insignificance of the viscous and the turbulent effects in the cases considered in this workshop.

However, if the relative size of the structure is small compared with the characteristic wave length, e.g. within the range of the application of the Morison's equation (usually < 0.2 characteristic wavelength), the viscous effects become important. The viscous effects are also significant under certain conditions, e.g. near the resonance region (e.g. [5]), the structure is subjected to the action of current (e.g. [9]). For such problems, the NS models may be necessary and the potential theory is not suitable, unless an appropriate artificial viscosity is applied (e.g. [5]). The artificial viscosity is often numerically calibrated using available experimental

results or reliable numerical predictions using the NS models. This obviously brings inconvenience to the numerical practices. However, the NS model is more time-consuming compared with the FNPT models, as evidenced by [8], not only because of the complexity of the governing equations of the NS models, but also due to the fact that a much finer mesh and smaller time step size are required by the NS models to achieve convergent results. For these reasons, the NS models are rarely applied in practices to model wave-structure interactions in large spatial-temporal domain. In many applications, the computational domain of the NS models is limited to a finite space near the structure (near field). This implies that one need to accurately specify the wave field near the structure on the wave generation boundary of the computational domain. A few tools (e.g. [10]) are available for specifying the wave conditions using different wave theories, e.g. the linear wave theory, Stokes wave theory, stream functions and high-order spectrum method (e.g. OceanWave3D). Broadly speaking, applying this tool with the NS models leads to a hybrid model combining these wave theories with the NS model using one-way zonal approach (spatially hierarchical, domain decomposition).

This paper contributes to the 2nd CCP-WSI Blind Test Workshop (https://www.ccp-wsi.ac.uk/blind_test_workshops), in which the cases with wave energy convertors (WECs) subjected to focusing waves with different wave conditions are set. The sizes of the WEC models used in these cases are considerably smaller than the characteristic wavelength. Furthermore, one of the WEC model is a cylinder with a moonpool at its centre. The viscous effects are expected to be significant. In order to take the advantages of the FNPT model on simulating large-domain wave propagation and the NS model on resolving small-scale viscous/turbulent effects near the structures, a hybrid model, qaleFOAM, which combines a two-phase NS model (OpenFOAM) and the FNPT based QALE-FEM using a spatially hierarchical approach, is applied to model the cases considered in the blind test.

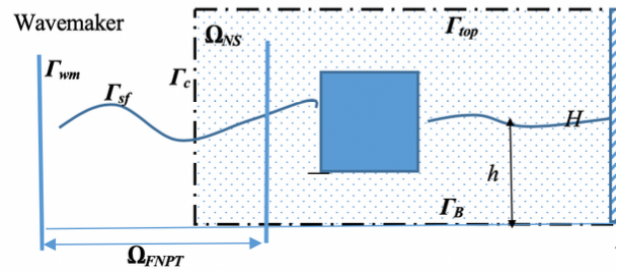

Fig. 1. Sketch of the domain decomposition and the coupling approach of the qaleFOAM.

II. Mathematical Formulae

A. qaleFOAM

The hybrid model, qaleFOAM, combines the QALE-FEM and OpenFOAM using a zonal approach. The details of the qaleFOAM hve been given in [9] but a summary is provided for completeness. The coupling strategy of the qaleFOAM is based on a domain decomposition method, and the two solvers are combined via a coupling boundary, Γ_c. Fig.1 illustrates the coupling of the FNPT and NS solvers. The FNPT domain (Ω_{FNPT}) starts from a location far away from the structures, where a wavemaker is used to generate the incoming wave. The length of the FNPT domain shall be sufficient to cover the inlet of the NS domain (Ω_{NS}). In this paper, one-way coupling is adopted and, therefore, the solution in Ω_{FNPT} is only used to provide an accurate wave condition at coupling boundary (inlet) of the Ω_N. For this purpose, the right end of Ω_{FNPT} is an absorption boundary and the self-adaptive wavemaker [11] is employed. In the FNPT domain, the QALE-FEM is used to solve the governing equations. The NS domain (Ω_{NS}) is bounded by the coupling boundary Γ_c at its left end (dashed line in Fig.1), seabed on the bottom, a pressure inlet/outlet boundary on the top, where the total pressure is specified as the atmospheric pressure, and the right end boundary. In the NS domain, the multiphase solver interDyMFoam, based on the finite volume method (FVM) with volume of fluid (VOF) technique for free surface identification, is used to model the multiphase flow properties. On the coupling boundary Γ_c, the velocity, pressure and wave elevation for the NS solver are provided by the QALE-FEM in the FNPT domain using,

$$\vec{u}(x,y,z) = \begin{cases} \nabla\varphi(x,y,z) & z \le \eta \\ \nabla\varphi(x,y,\eta) & z > \eta \end{cases} \tag{1}$$

$$p(x,y,z) = \begin{cases} -\rho_w \dfrac{\partial\varphi}{\partial t} - \rho_w \dfrac{\left|\vec{\nabla}\varphi\right|^2}{2} - \rho_w g z & z \le \eta \\ 0 & z > \eta \end{cases} \tag{2}$$

in which ρ_w is the density of the water; ϕ is the velocity potential; η is the free surface elevation. It is noted that the FNPT is a single-phase model only describing the water flow. In Eq. (1), the velocity of the flow above the free surface (i.e. the air phase) are specified by the corresponding water velocity on the free surface to ensure a smooth transition of the fluid velocity from the water phase to the air phase. In the NS domain, Ω_{NS}, a relaxation zone is applied near Γ_c, to suppress the reflected waves from the structures. The NS-solution f (velocity and pressure) in the relaxation zone is corrected by $f_{QALE}w + f_{NS}(1-w)$, where subscripts QALE and NS stand for QALE-FEM solution and NS solution respectively; w is the weighting function, which is 1 on Γ_c, and 0 on the other boundary of the relaxation zone.

B. Wave Generation and Absorption

The wave in the qaleFOAM is generated by the QALE-FEM in Ω_{FNPT} using a second order wavemaker theory [13] and propagates towards the ΩNS through the coupling boundary Γ_c,. To reproduce the wave conditions identical to that in the laboratory, a self-correction technique [4] is employed in this study. A summary of this technique is briefed here for completeness. The initial amplitudes and phases of the wave components driving the motion of the wavemaker are given by $a_i^0 = \sqrt{S(\omega i)\Delta\omega}$ and $\varphi^0 = k_i x_f - \omega_i t_f$, i = 1, 2…N, where x_f and t_f are the specified focusing location and time, respectively. While the target spectrum $S^*(\omega)$ and phase φ^* are obtained by applying FFT to the measured surface elevation $\eta^*(t, x_r)$ in laboratory, where x_r is

the gauge location. Then iterations are carried out in the following procedures:

(i) At the nth iteration, the wave maker motion is specified by using a_i^n and φ_i^n and the surface elevation $\eta^n(t,x_r)$ is recorded.

(ii) Correct the amplitude and the phase of each component by $a_i^{n+1} = a_i^n \sqrt{S^*(\omega_i)/S(\omega i)}$, $\varphi_i^{n+1} = \varphi_i^n + \varphi_m^*(\omega_i) - \varphi_m^n(\omega_i)$, where the subscription m denotes the average phase within the range $[\omega_i - \Delta\omega/2, \omega_i + \Delta\omega/2]$.

(iii) Calculate the error between $\eta^*(t,x_r)$ and $\eta^n(t,x_r)$ by using the formula, $Err = \max\{(\eta^* - \eta^n)^2/\eta^{*2}\}$. If Err is sufficiently small, the iteration stops; Otherwise, n = n + 1, go to step (i).

On the right end boundary of the NS domain, a fully absorption of the reflected wave from this boundary or a freely passage of the incoming wave is expected. In our previous paper [9], this boundary was treated in the same way as the left end and Ω_{FNPT} covers the entire Ω_{NS}. The numerical investigation in [9] has demonstrated the effectiveness of this approach for a satisfactory absorption of the reflected waves from this boundary. However, in this paper, the improved passive wave absorber [12] is employed and a summary will be given herein.

In the improved passive wave absorber technique, it is assumed that within a short period, e.g. at the scale of a time step of the NS simulation, any wave elevation at the absorption boundary can be reasonably fitted using a sine or cosine function,

$$\tilde{\eta}(t) = \tilde{A}(t)cos(\tilde{\psi}(\omega,t)) \tag{3}$$

in which ψ is the wave phase and the heading "~" means the instantaneous values during a short period. consequently, the instantaneous horizontal velocity may be expressed by

$$\tilde{u}_h(t) = \tilde{\omega}(t)\frac{\cosh\left(\tilde{k}(t)(z+d)\right)}{\sinh\left(\tilde{k}(t)d\right)}\tilde{\eta}(t) + \tilde{u}_h^n(t) \tag{4}$$

where $\tilde{u}_h^n(t)$ is caused by the nonlinear and/or transient effect. $\tilde{\eta}(t)$ can be real-time sampled in the time-domain simulation, if one can track the instantaneous $\tilde{\omega}(t)$, the linear wave dispersion can give the instantaneous wave number $\tilde{k}(t)$. In this paper, the Extended Kalman Filter (EKF) is used to track the instantaneous $\tilde{\omega}(t)$ using the on-board sampled elevation $\tilde{\eta}(t)$. The term $\tilde{u}_h^n(t)$ obviously depends on the wave condition, e,g. for the steady linear wave, $\tilde{u}_x(t)$=0, and is hardly descried using a general equation. In this paper, it is ignored and, eventually, the boundary condition specified in the NS solver is

$$\vec{U}_h(t) = \tilde{\omega}(t)\frac{\cosh\left(\tilde{k}(t)(z+d)\right)}{\sinh\left(\tilde{k}(t)d\right)}\tilde{\eta}(t)\cdot\vec{n}_h \tag{5}$$

$$\frac{\partial U_z}{\partial z} = 0 \tag{6}$$

It is worth of noting that ignoring the transient and nonlinear term $\tilde{u}_h^n(t)$ may not lead to significant accumulated error in the time domain simulation. Since the error caused by this term is expected to be included in the on-board $\tilde{\eta}(t)$ at the next time step and will be fully or partially absorbed in the following time steps. However, it is expected to see a reduction of the absorption efficiency as the increase of the wave steepness. One may apply a damping zone with this technique to improve the efficiency. In such a case, the target of the damping zone is not to completely suppress the wave energy but the nonlinear components (typically with higher wave frequencies or shorter wavelength compared with the fundamental wave components). Consequently, the size of the damping zone and the damping coefficient can be significantly reduced. It shall be noted that this technique does not requires the motion of the computational mesh, bringing a significant benefit to the CFD simulation adopting Eulerian (fixed) grid.

The effectiveness of the self-correction wave generation technique and the improved passive wave absorber have been demonstrated in [4] and [12], respectively, and readers can refer to these references for further details.

C. *Motion of WECs*

The involvement of the floating bodies requires the governing equation for the 6DoF motions of rigid body is required. In the OpenFOAM, Newton's 2nd law is employed to govern the time variations of the orientation tensor. In the qaleFOAM, new module is developed to apply the Newton's 2nd law in the body-fixed coordinate system and the rotation is described directly using the Euler angles $\boldsymbol{\theta}(\alpha,\beta,\gamma)$,

$$[M]\dot{\boldsymbol{U}}_c = \boldsymbol{F} \tag{7}$$

$$[I]\dot{\boldsymbol{\Omega}} + \boldsymbol{\Omega}\times[I]\boldsymbol{\Omega} = \boldsymbol{N} \tag{8}$$

$$\frac{d\boldsymbol{S}}{dt} = \boldsymbol{U}_c \tag{9}$$

$$[B]\frac{d\boldsymbol{\theta}}{dt} = \boldsymbol{\Omega} \tag{10}$$

where $\boldsymbol{F}$ and $\boldsymbol{N}$ are the external forces and moments acting on the floating body; $\boldsymbol{U}_c$ and $\dot{\boldsymbol{U}}_c$ are translational velocity and acceleration of its gravitational centre (rotational centre); $\boldsymbol{\Omega}$ and $\dot{\boldsymbol{\Omega}}$ are its angular velocity and acceleration; S is the translational displacement. In Eq. (7) and (8), $[M]$ and $[I]$ are the mass and inertia-moment matrix, respectively. $[B]$ in Eq. (10) is the transformation matrix formed by Euler angles and defined as

$$[B] = \begin{bmatrix} cos\beta cos\gamma & sin\gamma & 0 \\ -cos\beta sin\gamma & cos\gamma & 0 \\ sin\beta & 0 & 1 \end{bmatrix} \tag{11}$$

It is easy to deduce that $\boldsymbol{\Omega}\times[I]\boldsymbol{\Omega} = \boldsymbol{0}$ and $[B]$ is a unit matrix for the cases with 3 degree of freedom, i.e. surge, heave and roll.

III. CCP-WSI BLIND TEST

For the CCP-WSI blind test considered here, the experiment was performed in the wave basin at the University of Plymouth, which features 35 m in length, 15.5m in width and 3m in depth, as sketched in Fig. 2(a). Flap wave paddles are installed to generate three-dimensional waves. The temporal variation of surface elevations at various locations is recorded by 13 wave gauges (WG) with sampling frequency of 128Hz. The distribution of the gauges is sketched in Fig.2(b). Three wave conditions are used and summarized in Tab. 1. Two models of point-absorber WECs with a specific mooring system are initially placed at where WG5 is located. The geometries of these models are illustrated in Fig.3, the mass (m), moments of inertias (I_{xx}, I_{yy} and I_{zz}) at the centre of the mass (CoM) are summarised in Tab.2, in which Z_{COM} stands for the vertical distance from the CoM to the bottom of the models. For both models, the mooring used is a linear spring with a stiffness of 67 N/m and a rest length of 2.224m. More details can be found at www.ccp-wsi.ac.uk.

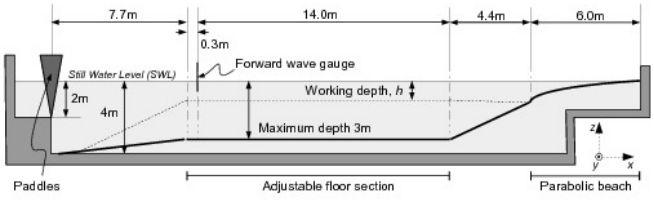

(a)

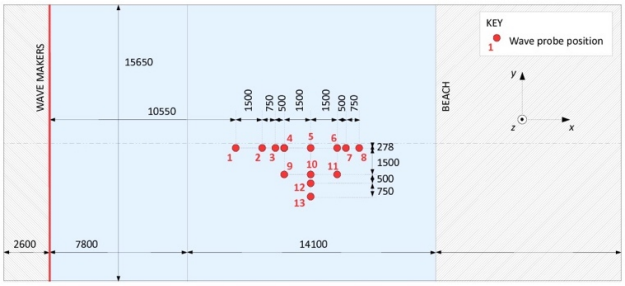

(b)

Fig. 2. (a) Sketch of the COAST Laboratory Ocean Basin dimensions; (b) Wave probe layout (all dimensions in mm)

TABLE I
WAVE CONDITIONS

Case ID	An(m)	fp(Hz)	h(m)	Hs(m)	kA
1BT2	0.25	0.3578	3.0	0.274	0.128778
2BT2	0.25	0.4	3.0	0.274	0.160972
3BT2	0.25	0.4382	3.0	0.274	0.193167

TABLE 2
MASS AND MOMENT OF INERTIA

Model	m(kg)	Z_{COM}(m)	I_{xx}(kgm²)	I_{yy}(kgm²)	I_{zz}(kgm²)
1	43.674	0.191	1.620	1.620	1.143
2	61.459	0.152	3.560	3.560	3.298

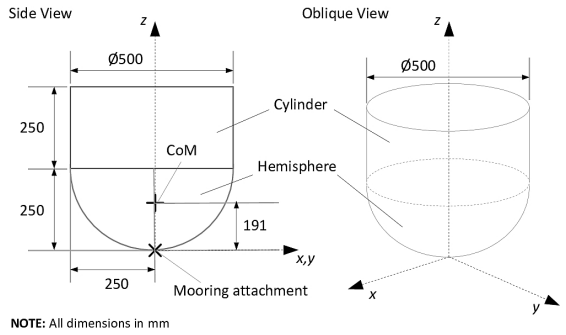

(a) Hemispherical-bottomed buoy (Model 1)

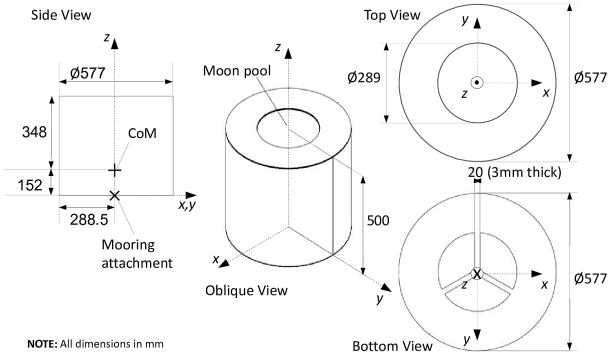

(b) Cylinder with moon-pool (Model 2)

Fig. 3. Geometries of two WEC models (all dimensions in mm)

D. Wave Generation and Absorption

For all cases, the corresponding empty-tank simulation are carried out to examine whether the target waves are generated properly. In the empty tank test, the length of the FNPT domain (Ω_{FNPT}) is 50m and origin of the x-coordinate starts from the wavemaker; the NS domain (Ω_{NS}) starts at x = 11.55m, between WG1 and WG2, and ends at x = 17.55m, where WG8 is placed. The height of Ω_{NS} are 6m. The width of Ω_{NS} is 3m. The wave is generated using the self-correction wavemaker in the left end of the Ω_{FNPT} aiming to reproduce the same time history of the wave elevations recorded at WG5, due to the fact that the seabed and the wavemaker geometry are not clearly specified and the wavemaker motion time histories are not recorded. At the outlet of the NS domain, the improved passive wave absorber [12] is employed. For all cases, a laminar model is specified as the turbulence properties.

The comparisons of the wave elevations at different wave gauges between the qaleFOAM results and the experimental data are shown in Figs. 4-6, which confirm a satisfactory reproduction of the target waves in the numerical wave tank, although the tank geometry and the wavemaker used in the qaleFOAM are different from the experiment. Even at WG8, i.e. the end of the Ω_{NS}, the qaleFOAM results fairly agree with the experimental data, suggesting a satisfactory effectiveness of the present wave passive wave absorber.

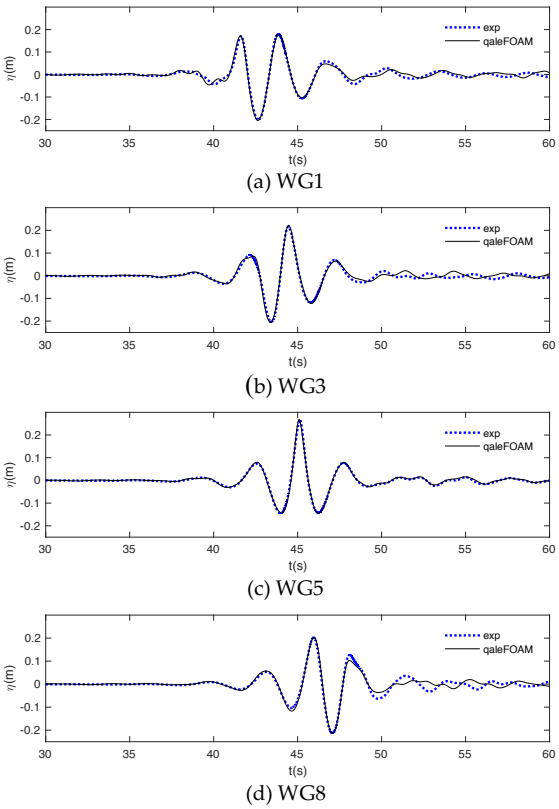

(a) WG1

(b) WG3

(c) WG5

(d) WG8

Fig. 4. Comparison of the wave elevation recorded at different locations (case 1BT2, empty tank test, ds_h = 0.05m, ds_v = 0.0175m)

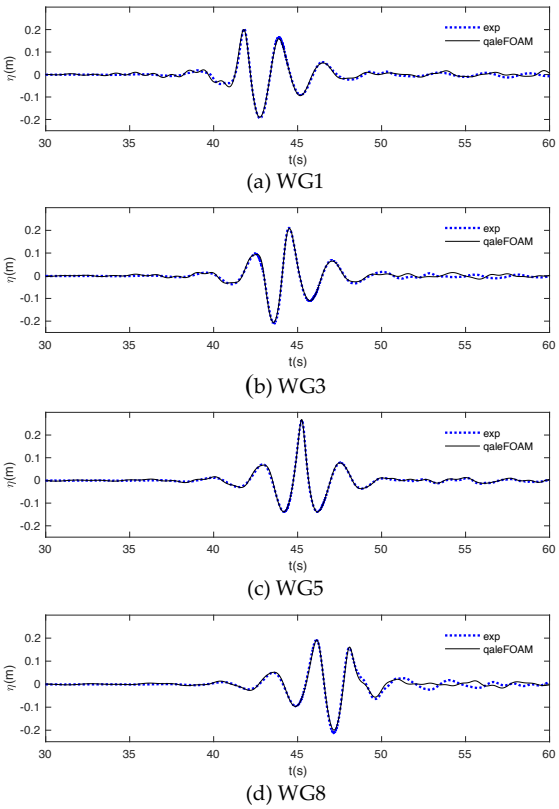

(a) WG1

(b) WG3

(c) WG5

(d) WG8

Fig. 5. Comparison of the wave elevation recorded at different locations (case 2BT2, empty tank test, ds_h = 0.05m, ds_v = 0.0175m)

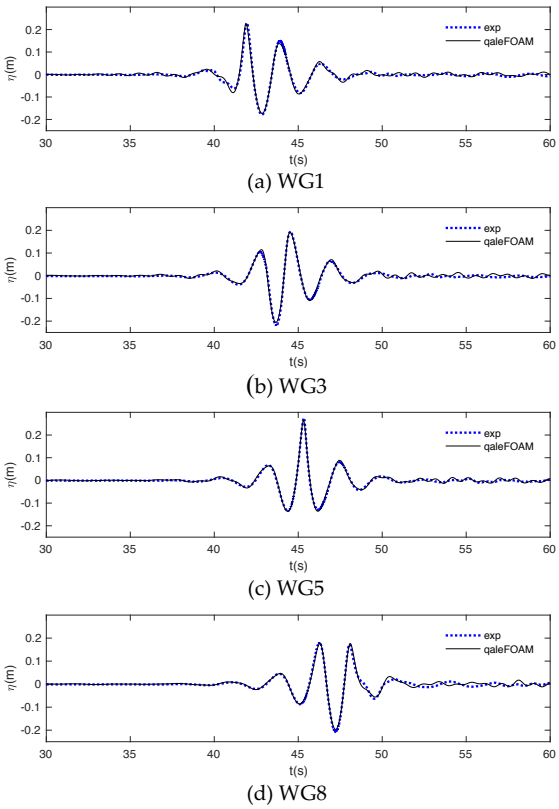

(a) WG1

(b) WG3

(c) WG5

(d) WG8

Fig. 6. Comparison of the wave elevation recorded at different locations (case 3BT2, empty tank test, ds_h = 0.05m, ds_v = 0.0175m)

TABLE 3
COMPUTATIONAL MESH

Model	Mesh	ds_h(m)	ds_v (m)	N_t (M)	N_s
1	Finest	0.04	0.015	1.550	10348
1	Fine	0.05	0.0175	0.956	7512
1	Medium	0.06	0.02	0.613	5346
1	Coarse	0.08	0.02	0.358	3882
2	Finest	0.04	0.015	1.549	20128
2	Fine	0.05	0.0175	0.937	13920
2	Medium	0.06	0.02	0.612	9840
2	Coarse	0.08	0.02	0.376	7244

E. Convergent tests

The results shown in Figs. 4-6 are obtained in a wave tank without WECs, i.e. the empty tank test. Corresponding convergent tests have been carried out to confirm that the results are convergfent. For the cases with WECs, convergent tests are also carried out. For each WEC model, four sets of computational mesh are generated using the snappyHexMesh tool and adopted in the convergent test. ds_h, ds_v , the total number of grid, N_t, and the number of grid on the structure surface, N_s, are summarised in Table 3. In order to capture the nonlinear wave-structure interaction near the structure, the mesh near a confined zone surrounding the WEC with a radius of 0.5m is refined. One example of the mesh near the WEC is illustrated in Fig. 7. The corresponding comparisons of the motions of the WEC and the mooring force are demonstrated in Fig.8 and Fig. 9, from which it is observed that the present results with three sets of

mesh agree with others. Further tests on other wave conditions lead to a similar conclusion that the Medium mesh may be sufficient to achieve convergent predictions on the WEC motions and the mooring force. The corresponding results are not shown in this paper to save the space.

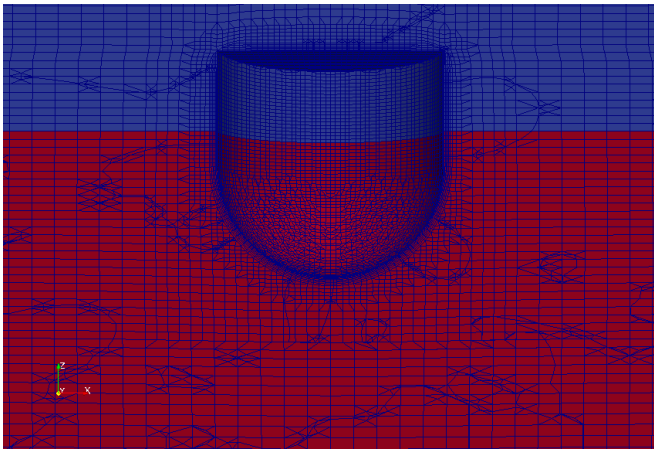

Fig. 7. Illustration of the computational mesh near the WEC (Model 1, ds_h = 0.05m, ds_v = 0.0175m, red: water; blue: air)

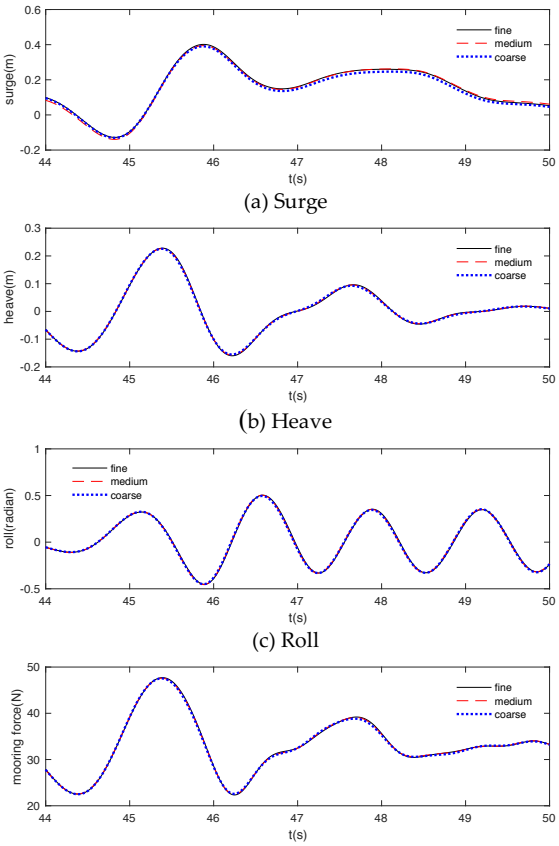

(a) Surge
(b) Heave
(c) Roll
(d) Mooring force

Fig. 8. Comparison of the WEC motions and mooring force in the cases with different mesh sizes (case 3BT2, Model 1)

A. *Responses of WECs in Focused Waves*

By using the medium mesh, the motions of the WECs subjected to three wave conditions are numerically simulated and analysed in this section.

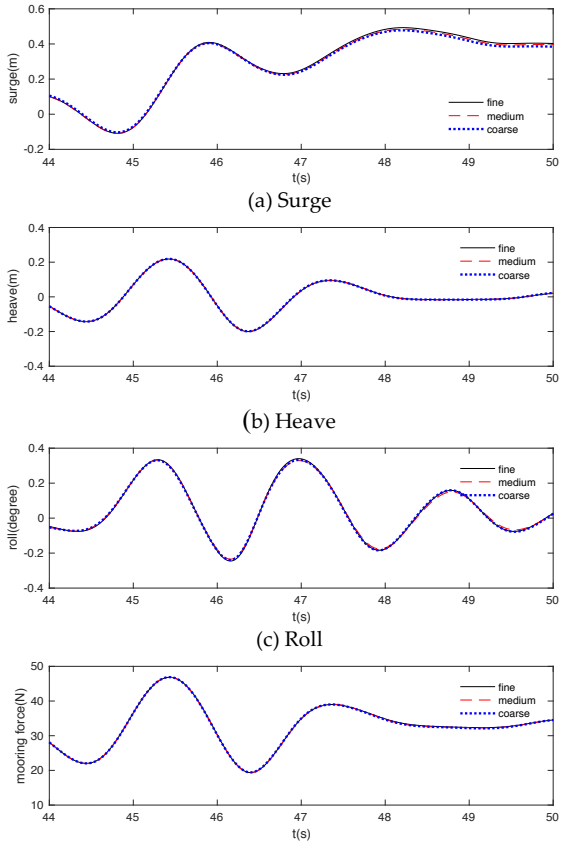

(a) Surge
(b) Heave
(c) Roll
(d) Mooring force

Fig. 9. Comparison of the WEC motions and mooring force in the cases with different mesh sizes (case 3BT2, Model 2)

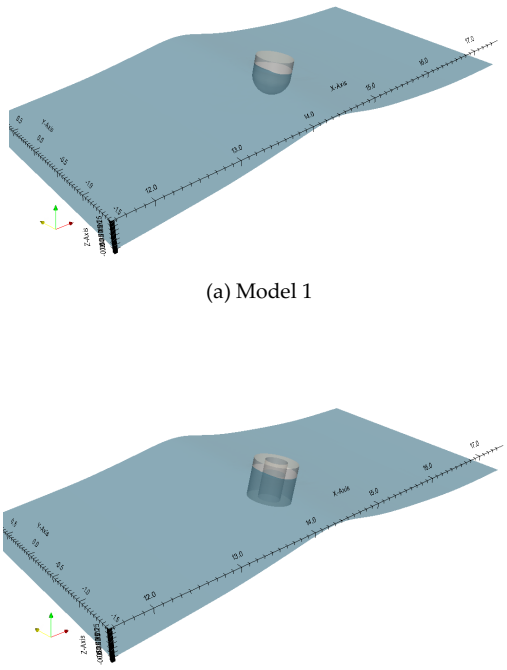

(a) Model 1
(b) Model 2

Fig. 10. Wave elevations near the WECs at t = 45s (case 2BT2)

For demonstration, Fig.10 and Fig. 11 illustrates the wave elevations near the WECs at two instants around the focusing time, i.e. t = 45s and t = 46s, in the cases with

wave condition 2BT2. As expected, the presences of the WECs do not seem to disturb the surrounding wave field, confirming to the typical feature of slender bodies (the sizes of the WECs considerably smaller than the characteristic wavelength).

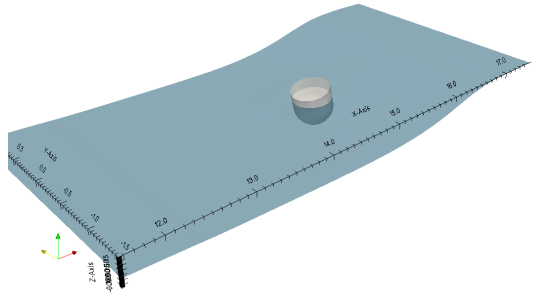

(a) Model 1 t=46s

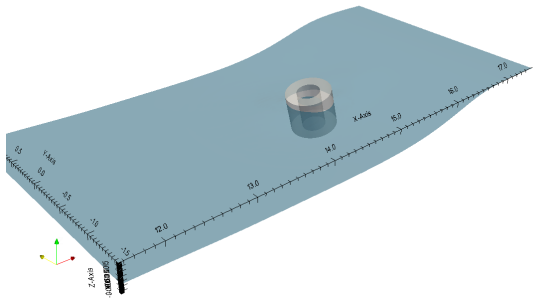

(b) Model 2

Fig. 11. Wave elevations near the WECs at t=46s (case 2BT2)

The motions of the WECs and the mooring force acting on the WECs in the case shown in Figs. 10 and 11 are illustrated in Fig.12. It is found that the profiles of the heave motions largely follow the wave motion (Fig. 5(c)). This may suggest a linear heave motion response. This can be confirmed by Fig. 13, which displays the amplitude spectra of the WEC motions and the corresponding wave spectrum at WG5 where the WECs are located. In Fig. 13, the spectra are obtained using the time histories using the time window of 35.3 – 50.3s and a sampling frequency of 128Hz. As observed from Fig.13(b), the amplitude spectra of the wave and the heave motion are very close, suggesting a linear heave response to the incident wave. However, the surge motion and the roll motion exhibit different features from the expected wave at the WEC sites. Specifically, the surge motions suffer from a long-period oscillation after the focused wave crest passes the WECs at $t \approx 45s$ (Fig. 12 (a)), whereas the roll motion exhibits a high-frequency response, which is gradually supressed in the case with Model 2. These are confirmed by the corresponding spectrum analysis shown in Fig. 13 (a) and (c), respectively.

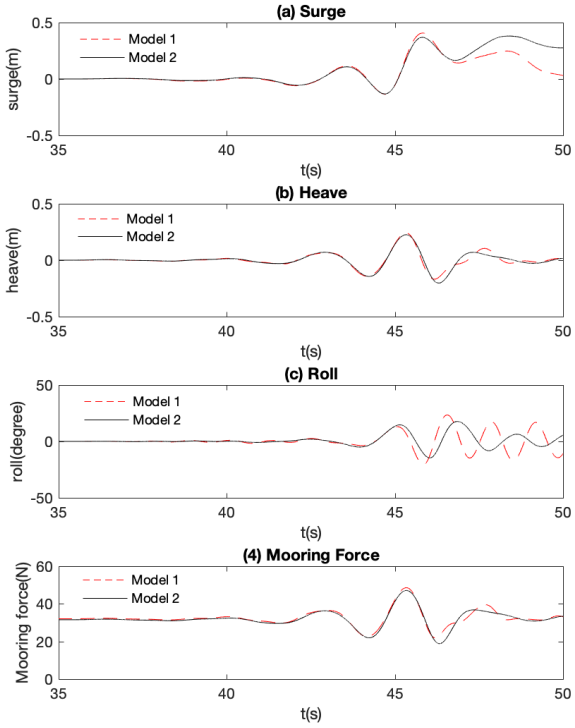

Fig. 12. Time history of the WEC motions and mooring forces (case 2BT2)

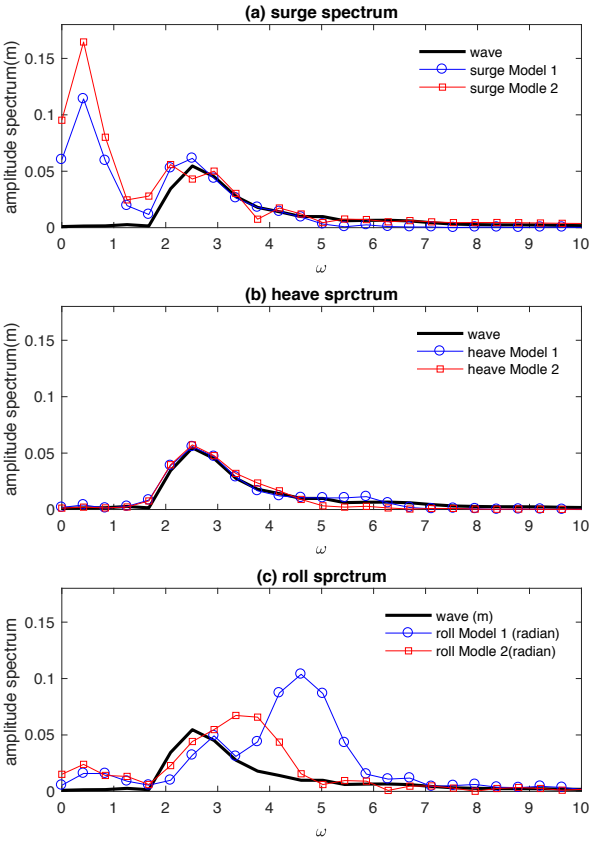

Fig. 13. Motion spectra (case 2BT2)

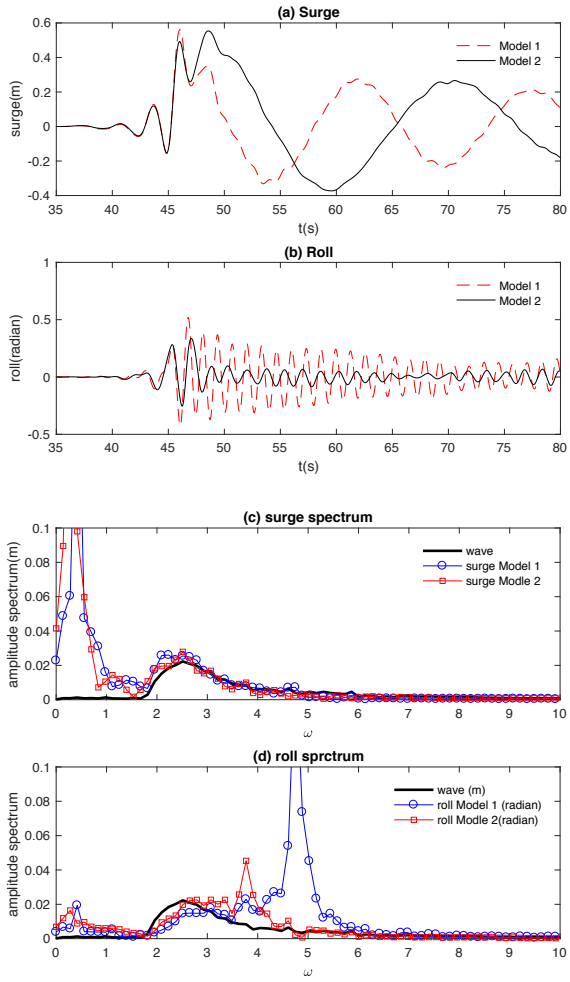

Fig. 14. Time history of the surge (a), roll (b) and the corresponding amplitude spectrum(case 2BT3 Blind Test 3 https://www.ccp-wsi.ac.uk/blind_test_workshops)

For the surge motion (Fig. 12(a) and Fig. 13(a)), the restoring force is primarily the mooring force and therefore the natural frequency can be roughly estimated using $\sqrt{k/m}$, yielding 1.24rad/s and 1.04 rad/s for Model 1 and 2, respectively. The low frequency responses shown in Fig. 13(a) corresponds to $\omega \approx 0.5$ rad/s may be caused by nonlinear transient effects and is expected to be supressed by the viscous effects slowly. Due to the fact that the all cases presented in this paper are terminated at t = 50.3s, longer durations of the surge motion are not recorded. However, cases using the same WEC models subjected to a similar wave condition are modelled in other Blind Test Workshop (Blind Test 3 (https://www.ccp-wsi.ac.uk/blind_test_workshops), results may be useful to discuss this issue. Some results are shown in Fig. 14, for this purpose. As confirmed by Fig. 14(a), the low-frequency oscillations are gradually supressed. The corresponding spectrum shown in Fig. 14(c), which is obtained using the time histories ranging from 35.3 to 80.3s, identifies the corresponding responses near the natural frequencies of the surge motion for both models, i.e. noticeable peak around 1.24rad/s and 1.04 rad/s, respectively for Model 1 and 2. For the roll motion, its spectrum shown in Fig. 13(c) exhibits peaks around $\omega \approx$ 3.5 rad/s and 4.5 rad/s for Model 1 and 2, respectively. These are believed to be the corresponding natural frequencies, as confirmed by the case shown in Fig. 14(d). Other than these, noticeable peaks near $\omega \approx 0.5$ rad/s are also identified, perhaps caused by the interaction between the surge and the roll motion.

In addition to the wave condition 2BT2, other wave conditions summarised in Table 1 are also considered in this paper. The detailed analyses on the spectrum are not given but the time histories of the motions and the mooring forces are displayed in Figs. 15-16 for completeness.

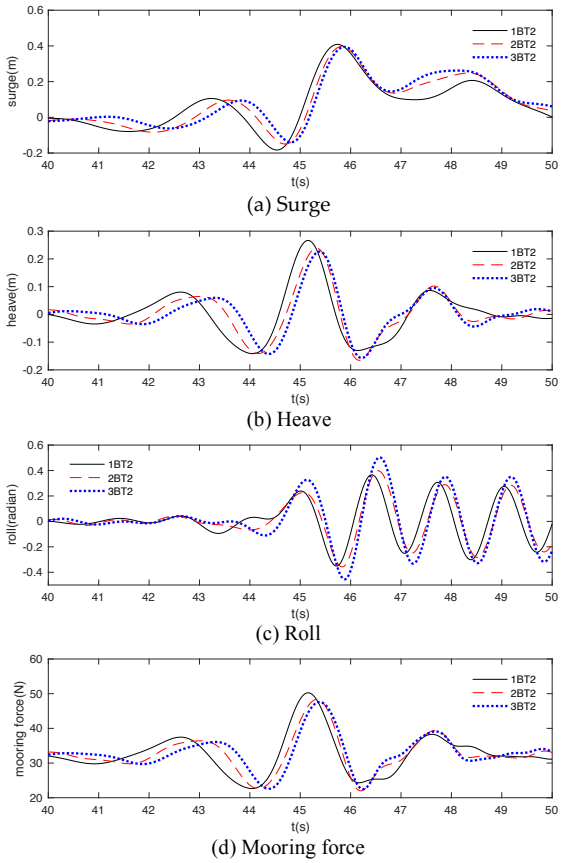

Fig. 15. Motions of WEC Model 1 and associated mooring forces subjected to different wave conditions

IV. CONCLUSION

In this paper, the qaleFOAM are used to numerically simulate the cases specified by the CCP-WSI Blind Test 2. All wave conditions summarised in Table 1 have been considered but some results are not presented here to avoid overlength. The effectiveness of the qaleFOAM on modelling focused wave group is assessed by comparing the wave elevations in the empty tank tests, in which the WEC models are not placed. The results confirm a promising accuracy of the qaleFOAM on modelling highly nonlinear water waves. In addition, the convergence test has demonstrated a good convergence property in terms of predicting the motions of the WECs and the associated mooring forces. Due to the fact that the experimental data will be released during the workshop, further comparison with the experimental data is not

given, but a preliminary assessment of the characteristics of the WEC motions subjected to focused wave groups is presented.

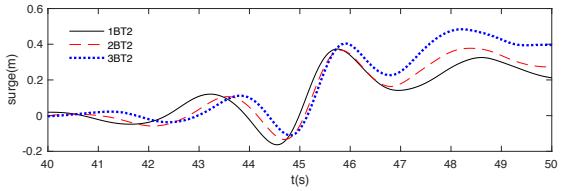

(a) Surge

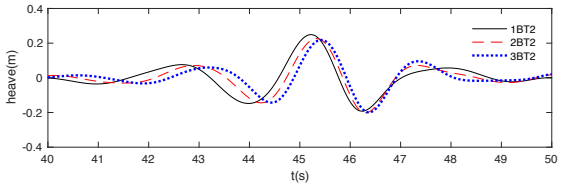

(b) Heave

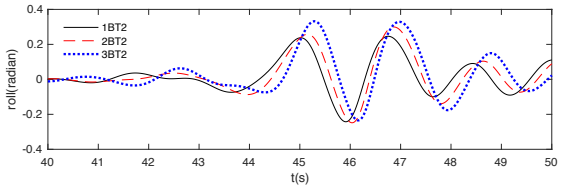

(c) Roll

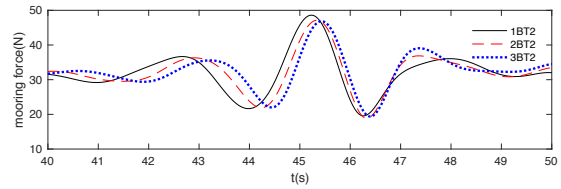

(d) Mooring force

Fig. 16. Motions of WEC Model 2 and associated mooring forces subjected to different wave conditions

ACKNOWLEDGEMENT

The authors gratefully acknowledge the financial support of EPSRC projects (EP/M022382, EP/N006569 and EP/N008863) and UKIERI-DST project (DST-UKIERI-2016-17-0029).

REFERENCES

[1] P. S. Tromans, A.R. Anaturk, and P. Hagemeijer, "A new model for the kinematics of large ocean waves – application as a design wave," in *The First International Offshore and Polar Engineering Conference*. Edinburgh, UK, 1991.

[2] Q.W. Ma, G.X. Wu, and R. Eatock Taylor, "Finite element simulation of fully nonlinear interaction between vertical cylinders and steep waves. Part 1: Methodology and numerical procedure ", *Journal for Numerical Methods in Fluid* , Vol. 36, pp. 265-285, 2001.

[3] Q.W. Ma, and S. Yan, "Quasi ALE finite element method for nonlinear water waves ," *Journal of Computational Physics*, Vol. 212, pp. 52-72, 2006.

[4] Q.W. Ma, S. Yan, D. Greaves, T. Mai, and A. Raby, "Numerical and experimental studies of Interaction between FPSO and focusing waves," in *The Twenty-fifth International Ocean and Polar Engineering Conference*, Kona, Hawaii, USA, 2015.

[5] S. Yan, and Q.W. Ma, " Numerical simulation of fully non-linear interaction between steep waves and 2D floating bodies using the QALE-FEM method," *Journal of Computational Physics*, Vol. 221, pp.666–692, 2007.

[6] Q.W. Ma, and S. Yan, "QALE-FEM for numerical modelling of non-linear interaction between 3D moored floating bodies and steep waves", International Journal for Numerical Methods in Engineering , 2009, Vol.78, pp. 713-756.

[7] S. Yan, Z.H. Xie, Q. Li, J.H. Wang, Q.W. Ma, T. Stoesser, "Comparative numerical study on focusing wave interaction with FPSO-like structure," *International Journal of Offshore and Polar Engineering* (in press), 2019.

[8] E. Ransley, S. Yan, S. Brown, T. Mai, D. Graham, D. Greaves, Q.W. Ma, P.H. Musiedlak, A.P. Engsig-Karup, C. Eskilsson, Q. Li, J. H. Wang, Z. Xie, V. Sriram, T. Stoesser, Y. Zhuang, Q. Li, D. Wan, G. Chen, H. Chen, L. Qian, Z. Ma, D. Causon, C. Mingham, I. Gatin, H. Jasak, V. Vukcevic, S. Downie, P. Higuera, E. Buldakov, D. Stagonas, Q. Chen, J. Zang, "A blind comparative study of focused wave interactions with a fixed FPSO-like structure (CCP-WSI Blind Test Series 1)," *International Journal of Offshore and Polar Engineering* (in press), 2019.

[9] Q. Li, J.H. Wang, S. Yan, J.Y. Gong, and Q.W. Ma "A Zonal Hybrid Approach Coupling FNPT with OpenFOAM for Modelling Wave-Structure Interactions with Action of Current", *Ocean System Engineering*, Vol. 8, pp. 381-407, 2018.

[10] N.G. Jacobsen, D.R. Fuhrman, and J. Fredsøe, J "A wave generation toolbox for the opensource CFD library: OpenFoam", *International Journal for Numerical Methods in Fluid*, Vol. 70, 1073-1088, 2011.

[11] S. Yan, Q.W. Ma, J.H. Wang, and J. Zhou, "Self-adaptive wave absorbing technique for nonlinear shallow water waves," in *ASME 35th International Conference on Ocean, Offshore and Arctic Engineering*, Busan, South Korea,2016

[12] J.X. Wang, J.H. Wang, S. Yan, Q.W. Ma, and G.H. Xia, "An improved passive wave absorber for FNPT-NS solver," submitted to *the Twenty-ninth International Ocean and Polar Engineering Conference*, Honolulu, Hawaii, USA, 2019

[13] H.A. Schaffer, "Second-order wavemaker theory for irregular waves," *Ocean Engineering*, Vol. 23, 47-88, 1996.